ACS APPLIED MATERIALS & INTERFACES

www.acsami.org
Research Article

Fluidic Interface for Surface-based DNA Origami Studies

Miguel García-Chamé, Ivy Mayer, Leonie Schneider, Christof M. Niemeyer, and Carmen M. Domínguez*

Cite This: ACS Appl. Mater. Interfaces 2024, 16, 53489−53498

Read Online

ACCESS | Metrics & More | Article Recommendations | Supporting Information

ABSTRACT: Traditionally, the use of DNA origami nanostructures (DONs) to study early cell signaling processes has been conducted using standard laboratory equipment with DONs typically utilized in solution. Surface-based technologies simplify the microscopic analysis of cells treated with DON agents by anchoring them to solid substrates, thus avoiding the complications of receptor-mediated endocytosis. A robust microfluidic platform for real-time monitoring and precise functionalization of surfaces with DONs was developed here. The combination of controlled flow conditions with an upright total internal reflection fluorescence microscope enabled the kinetic analysis of the immobilization of DONs on DNA-functionalized surfaces. The results revealed that DON morphology and binding tags influence the binding kinetics and that DON hybridization on surfaces is more effective in microfluidic devices with larger-than-standard dimensions, addressing the low diffusivity challenge of DONs. The platform enabled the decoration of DONs with protein-binding ligands and in situ investigation of ligand occupancy on DONs to produce high-quality bioactive surfaces. These surfaces were used to recruit and activate the epidermal growth factor receptor (EGFR) through clustering in the membranes of living cancer cells (MCF-7) using an antagonistic antibody (Panitumumab). The activation was quantified depending on the interligand distances of the EGFR-targeting antibody.

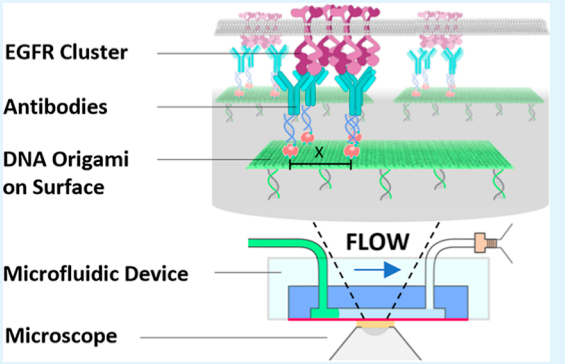

KEYWORDS: *DNA nanostructures, epidermal growth factor receptor, microfluidics, micropatterning, Panitumumab, surfaces*

INTRODUCTION

DNA-based platforms are gaining significance in both fundamental and applied biological and biomedical research. Notably, Rothemund's DNA origami nanostructures (DONs)[1] are pivotal, as they allow for the easy and efficient functionalization with proteins and other bioactive components at near-molecular resolution.[2,3] Numerous experimental studies demonstrate that DONs can be used to investigate the molecular mechanisms of cellular signaling cascades in biological processes such as cell adhesion and activation.[4−31] In many of these studies, bioactive DONs are introduced into the target cells as a soluble component. This method, suitable for various research questions, is straightforward and facilitates the cellular uptake of DON agents through different receptor-mediated processes. However, it can complicate the microscopic analysis of cells treated with DONs, as receptor-mediated endocytosis may overlap with the mechanisms being investigated, making analysis more challenging. Surface-based technologies offer an advantage here, as the DON agent can be anchored to a solid substrate and time- and spatially resolved microscopy analyses are easy to perform.[32] To this end, our group has developed the so-called "multiscale origami structures as interface for cells" (MOSAIC) technique,[5] in which top-down printed DNA patterns are used for DNA-directed immobilization of double-sided functionalized DONs carrying anchor strands and ligand patterns on the bottom and top of quasi-two-dimensional origami scaffolds, respectively. We have successfully used this methodology to study the early phase of the epidermal growth factor (EGF) signaling pathway.[5,14,19,30] A detailed comparison of prior studies on cell signaling processes with protein-decorated DONs, indicating whether they are used in solution or on surfaces and including the receptors studied, can be found in the Supporting Information (Table S1).

However, the production and characterization of DNA-patterned surfaces, as well as their application in microscopic cell studies, demand meticulous experimental handling of functionalized substrates. Ideally, this process should be automated. Microfluidic operating systems are well-suited for this purpose, serving as controlled reaction chambers and providing high-throughput arrays or micropositioning systems for biological experiments with precise control over temper-

Received: July 1, 2024
Revised: August 2, 2024
Accepted: August 16, 2024
Published: September 30, 2024

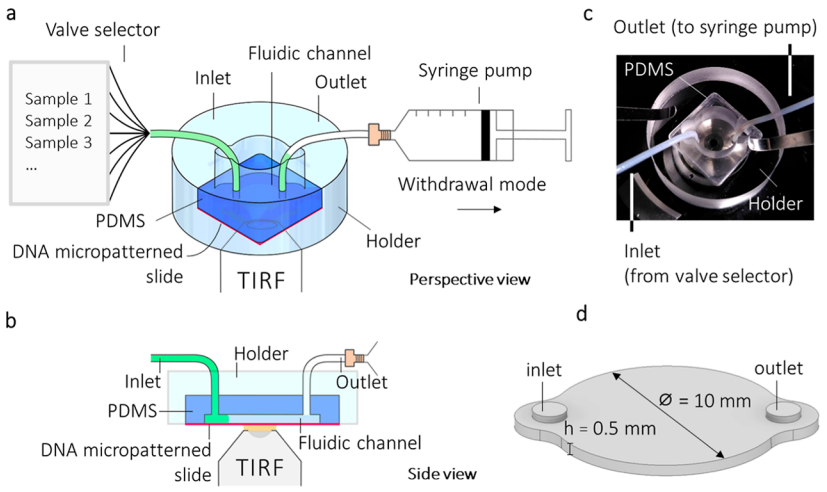

Figure 1. Microfluidic setup. (a) Perspective view scheme of the experimental setup. The fluidic device, the valve selector, and all samples were placed inside of the closed environment of the microscope (see Figure S1). (b) Side view scheme and (c) photograph of the device within the holder that enables to fix the chip on the microscope stage. (d) Design of the fluidic chamber.

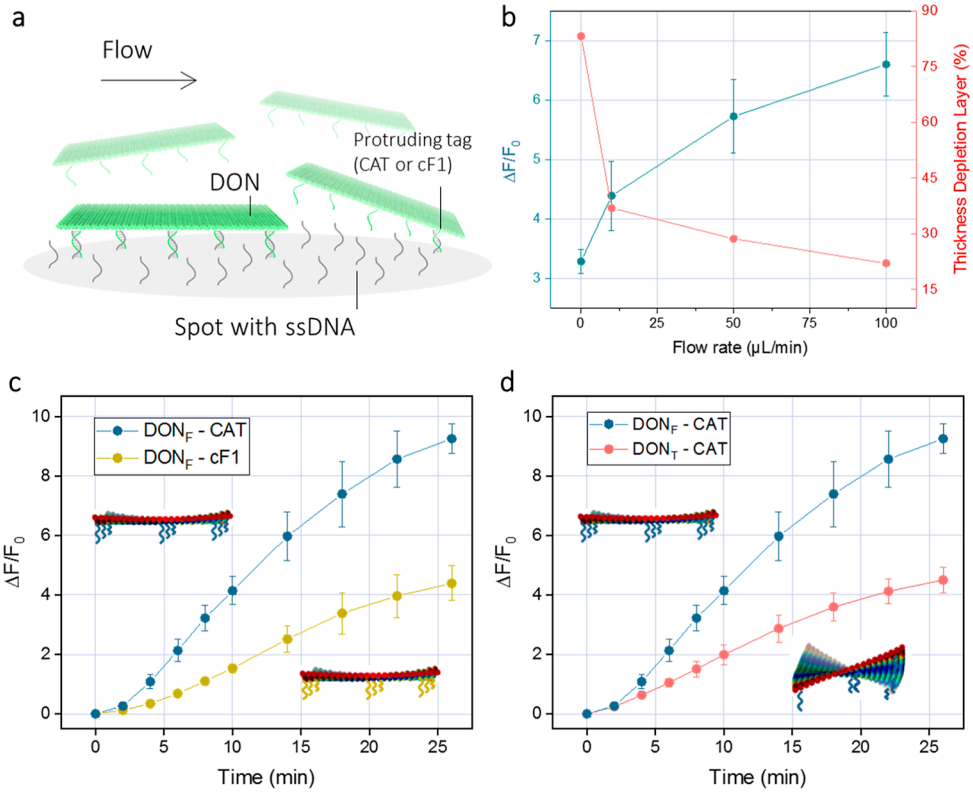

Figure 2. Characterization of DON hybridization. (a) Scheme for site-directed immobilization of DONs to spots presenting ssDNA under flow conditions. (b) End point hybridization levels measured through the relative fluorescence intensity $\Delta F/F_0$ at 26 min (left *y*-axis) and thickness of the depletion layers (right *y*-axis) versus flow rate. The depletion layer thickness was derived from COMSOL numerical simulations. For the 0 μL/min condition, only diffusive transport was considered. For other flow rates (10, 50, and 100 μL/min), both convective and diffusive transport were included in the simulation. The flown species was assumed to have a diffusion coefficient of 2×10^{-12} m^2/s, which is an estimation for molecular structures with hydrodynamic diameters of about 100 nm.[35] Figure S4 presents details of these simulations. (c) Relative fluorescence intensity $\Delta F/F_0$ values obtained over time for the hybridization of the flat DON_F with different protruding oligonucleotides (CAT or cF1). (d) Relative fluorescence intensity $\Delta F/F_0$ values obtained over time for the hybridization of the two structurally different DONs within the fluidic device, DON_F and DON_T, which contained the same protruding tags (CAT). All experiments were done in duplicates. Mean and SD are shown.

ature and flow rates.[32,33] Furthermore, the integration of microfluidics in DNA nanotechnology, particularly in the context of DNA-based molecular motors, has proven essential for overcoming the limitations associated with the accumulation of chemical components over time, leading to significant improvements in processivity and operational yields.[34] Building on these principles, our research focuses on the development of a microfluidic device system that integrates microscopy techniques with the benefits of microfluidics for the automated assembly and precise decoration of DONs on

https://doi.org/10.1021/acsami.4c10874
ACS Appl. Mater. Interfaces 2024, 16, 53489−53498

surfaces. These structures, assembled on micropatterned single-stranded DNA (ssDNA) surfaces, were used to initiate membrane-associated processes in living cells. We demonstrate the effectiveness of our user-friendly experimental platform by examining the DON-driven clustering of the EGF receptor (EGFR) and its impact on the behavior of MCF-7 cells.

RESULTS AND DISCUSSION

The microfluidic device was integrated into an upright total internal reflection fluorescence (TIRF) microscope to enable real-time monitoring of surface decoration with DONs and subsequent decoration with specific ligands. The setup consisted of (i) a microfluidic device with a fluidic chamber mounted on top of an 18 × 18 mm^2 glass surface containing a DNA micropattern, (ii) a valve selector (Valco Instruments) connected to all the required samples, and (iii) a semi-automated syringe pump (Cetoni) operating in withdrawal mode (Figure 1a). The fluidic chamber was made of polydimethylsiloxane (PDMS) using standard soft lithography microfabrication methods (see the Experimental Section). The glass-PDMS hybrid device was connected to the valve selector and syringe pump by conventional polytetrafluoroethylene (PTFE) tubings with fittings for fluid delivery (Figure 1b). To maintain controllable environmental conditions such as temperature and humidity, the device and the valve selector holding all samples for surface functionalization were placed inside the microscope housing. A holder was fabricated to fix the device on the microscope stage (Figure 1c). Figure S1a shows pictures of the complete setup. The fluidic chamber was designed as a circular chamber with a diameter of 10 mm and a height of 500 μm (Figure 1d) that results in a volume of approximately 47 μL. The glass substrate, onto which the PDMS structure was mounted, was chemically activated and used for immobilization of amino-modified ssDNA capture strands, as previously described.[5] Patterning was achieved through inkjet printing, creating a 5 × 5 mm^2 array of DNA spots, with each spot measuring approximately 80 μm in diameter and spaced 200 μm apart (Figure S1b).

In initial studies, the site-directed immobilization of DONs on the patterned surface was monitored over time to characterize the immobilization kinetics and optimize the preparation of high-quality DON surfaces for cell culture experiments (Figure 2a). For these studies, we used flat rectangular DONs (DON_F, 70 × 100 nm^2) designed with a twist correction. DON_F contained ssDNA strands that hybridize with complementary capture oligonucleotides bound to the glass surface and included fluorescent dye labels for detection via TIRF microscopy (see the Experimental Section and Figure S2 for DON designs).

Initially, we evaluated the utility of our platform by studying how flow rates affected the DON_F hybridization. Fluorescent signals from DON_F binding were monitored over time at flow rates of 0, 10, 50, and 100 μL/min. To evaluate the efficiency of the hybridization of different samples and process conditions, we quantified changes in fluorescence intensity over time relative to the initial background intensity ($\Delta F/F_0$). Figure 2b presents the end point hybridization levels at 26 min (left y-axis). Time-lapse TIRF images of fluorescent signal increase and hybridization curves over 26 min are shown in Figures S3 and S4a, respectively. The signal increase with the flow rate (Figure 2b) indicates that at low flow rates, our system is partially limited by diffusive mass transfer, which creates a depletion layer over the reactive surface.[36] The thickness of the depletion layers obtained by COMSOL numerical simulations is shown in the right y-axis of Figure 2b, with details in Figure S4b,c. Higher flow rates replenish the depleted region faster, yielding higher hybridization signals. The asymptotic behavior of the increase, stabilizing around 100 μL/min, indicates that this flow rate reflects real binding kinetics rather than mass transfer rates. However, a flow rate of 100 μL/min requires very large sample volumes of DONs, which would make the assay hardly affordable. Hence, 10 μL/min was chosen for further experiments. As we demonstrate below, the partial mass transfer limitations did not hinder the ability to distinguish the binding of different DONs.

Under flow conditions, we then studied the effect of protruding oligonucleotides on the hybridization kinetics by comparing DON_F with the nonrepetitive scrambled sequence (cF1) tags to those constructs with triplet repetitions (CAT) tags (see Experimental Section for sequences). Figure 2c shows the higher and faster binding achieved by DONs prepared with CAT compared to those with cF1 protruding tags at 10 μL/min. While the cF1 sequence follows a standard nucleation and zippering behavior, the CAT sequence, consisting of triple repeats, likely involves a "slithering" mechanism,[37] that leads to faster binding kinetics.

Traditionally, DONs used to interface with cell membranes and study the effects of ligand arrangements on receptor activation were inherently twisted.[5,30] We then compared the hybridization of these twisted DONs (DON_T) with their twist-corrected counterparts (DON_F). Figure 2d shows the relative fluorescence intensity over time during hybridization of DON_T and DON_F at 2 nM equipped with the same protruding tags (CAT). The equilibrium became visible at 22 min, with DON_F reaching hybridization levels approximately three times higher than DON_T. DON_T exhibits a large curvature (Figure S5), whereas the twist correction results in a flat structure of DON_F.[19] Thus, the twist in DON_T, which leads to a fluctuation of tags at different levels (see insets in Figure 2d) and makes the structure stiffer in the middle (Figure S5), explains the reduced hybridization efficiency. Additional experiments comparing DON_F and DON_T with cF1 tags as well as DON_T with either CAT or cF1 tags (Figure S6) confirmed these results.

To demonstrate the competitiveness of our system, we evaluated its performance against a well-established surface plasmon resonance (SPR) technique. Since DON_T production was discontinued, a DON variant with a higher aspect ratio, previously reported by our group as a molecular ruler for ligand positioning in cell studies,[30] was used in these experiments. Thus, we compared twisted (DON_{RT}) and flat (DON_{RF}) DON rulers (252 × 40 nm^2, Figure S7a,b) with identical protruding tags (CAT) and from the same batch using both our device and a Biacore X100 instrument. At the end of the association phase, SPR showed a 10% difference in hybridization efficiency of the two species, while our device revealed a 20% difference at the same time point, both showing higher hybridization for DON_{RF} (Figure S7c,d). Although this difference may arise from capture oligo density variations between the systems, the high velocities in the SPR chamber, 150 times greater than in our device, and the low diffusion coefficient of the flowing species likely contribute as well, as indicated by Péclet number (Pe) calculations (see Figure S7 for details and an extended discussion). The Pe indicates the relative contribution of convective and diffusive transport processes. The larger dimensions of our homemade micro-

https://doi.org/10.1021/acsami.4c10874
ACS Appl. Mater. Interfaces 2024, 16, 53489−53498

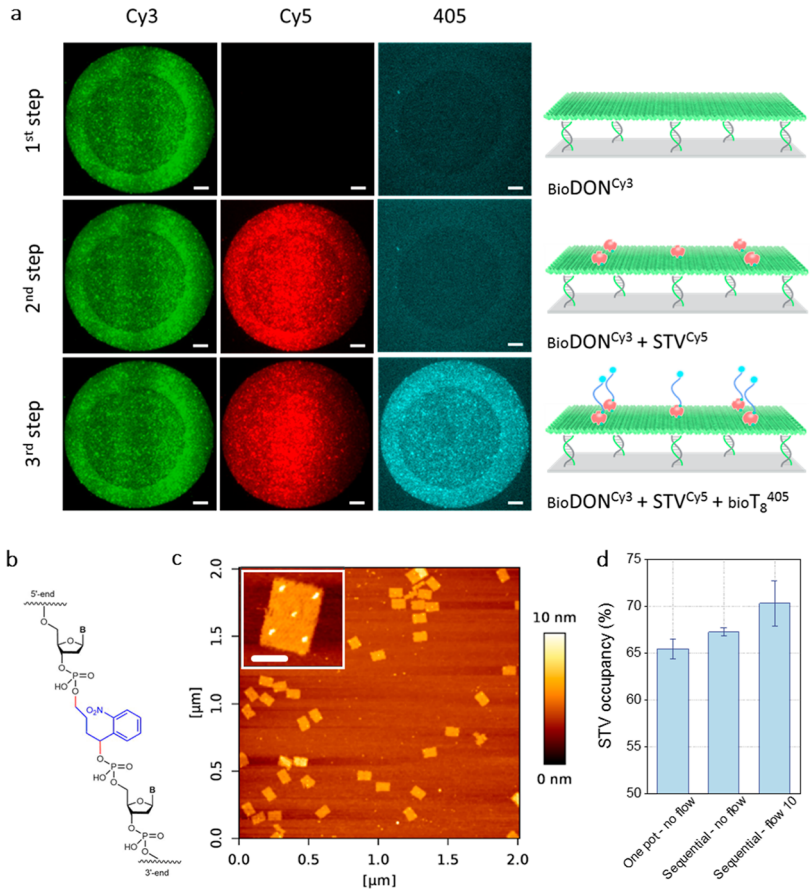

Figure 3. Surface decoration. (a) Sequential functionalization of the surface with (1st) Cy3-DON$_F$ presenting biotin ligands, (2nd) Cy5-STV that binds to the biotin ligands on DON$_F$, and (3rd) Dy405-labeled biotinylated ssDNA. The vertical dark lines that appear in the Cy3 and Cy5 channels are unavoidable artifacts of TIRF imaging. Scale bars: 10 μm. (b) Photocleavable linker introduced in the capture oligonucleotide sequence to release DON-STV constructs. (c) Atomic force microscopy (AFM) image of the released DON$_F$. The inset shows the "5 far" biotin-STV pattern. Scale bar: 50 nm. (d) STV occupancies measured for the released DON$_F$ by AFM analysis (n = 60−100) obtained under the following conditions: (i) one-pot incubation outside the fluidic chip; (ii) in the fluidic chip under static incubation conditions; and (iii) in the fluidic chip flowing the STV at 10 μL/min. Measurements were done in duplicates. Mean and SD are shown.

fluidic chambers lead to slower flow velocities that, combined with the low diffusivity of the DON, result in intermediate *Pe* (1 < *Pe* < 100). These facilitate efficient DON delivery to the reactive surface while maintaining some degree of mixing required to fully reach the surface. In contrast, the smaller SPR fluidic chamber results in higher flow velocities and, thus, high *Pe* (>100), which cause the DON to not have sufficient time to reach the reactive surface by diffusion over the last microns. This influence of *Pe* for biosensors has been discussed in the literature,[38] for an extended discussion, see Figure S7. Overall, these results confirmed that flat, twist-corrected DONs exhibit higher hybridization efficiency than twisted DONs, and they suggest that flow devices with larger dimensions might be more suitable for characterizing the binding kinetics of low-diffusivity species than classical microfluidic techniques with smaller reaction chambers.

With the aim to create high-quality interfaces with nanoscale biofunctional patterns for cell studies, we sequentially decorated the surface-bound DONs with active biomolecules. Specifically, we tested the functionalization of the surface with DON$_F$, streptavidin (STV), and biotinylated DNA to demonstrate a three-step decoration process via fluorescent detection (Figure 3a). To this end, some of the DON staples were first modified to include biotin ligands protruding upward, which served as a base to immobilize additional biomolecules (see the Experimental Section and Figure S2). The nanopattern of biotin ligands on the DON$_F$ used for these experiments corresponds to the so-called "5 far" configuration, shown in Figure S2e. Figure 3a shows representative fluorescence images of the successful specific sequential decoration of the surface with Cy3-DON$_F$ presenting biotin ligands, Cy5-STV binding to the biotins on the DON$_F$, and Dy405-labeled biotinylated ssDNA binding to the immobilized STV, respectively. This decoration process demonstrates the capability of our platform to create high-quality, biofunctional nanoscale patterns for biological applications. To further validate the efficiency of nanopattern decoration on the DON$_F$, we analyzed the STV occupancy after sequential fluidic incubation.

To achieve this, we incorporated a photocleavable linker (Figure 3b) within the capture oligonucleotide anchored to the surface. Following incubation with the DON$_F$ and the STV, or the DON$_F$/STV construct, the surface was irradiated with UV light (λ = 312 nm) to release the constructs, which were then analyzed with AFM (Figure S8). Figure 3c shows AFM images of the released DON$_F$ with the "5 far" pattern after STV decoration. Using this approach, we compared the STV occupancy under three different incubation conditions: (i)

https://doi.org/10.1021/acsami.4c10874
ACS Appl. Mater. Interfaces 2024, 16, 53489−53498

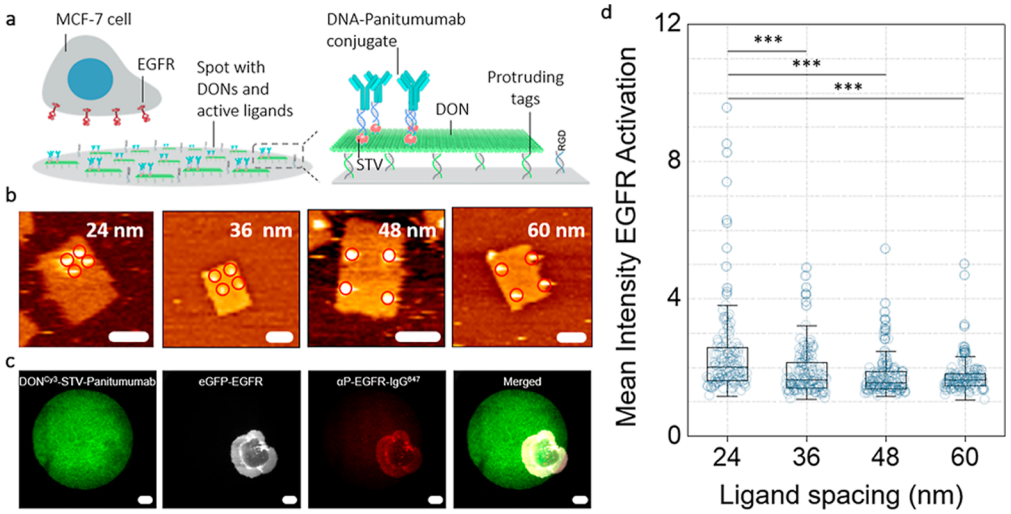

Figure 4. DON_F with Panitumumab-DNA conjugates for EGFR activation studies. (a) Scheme for MCF-7 cells interacting with a functionalized spot. The active surface included biofunctional DONs to target EGFR and RGD motifs to guarantee integrin-mediated cell adhesion. The DONs contained: (i) STV bound through bidentate biotinylated linkers,[19] (ii) Panitumumab-DNA conjugates with double biotin groups on the 5′ end to fully cover the remaining STV binding sites, and (iii) a complementary oligonucleotide to the conjugate to increase DNA rigidity and ensure precise ligand positioning. (b) AFM topographic images of DONs presenting STV at lateral interligand spaces of 24, 36, 48, and 60 nm. Scale bars: 50 nm. (c) Representative TIRF image of an MCF-7 cell on top of a functionalized spot with ligand-decorated Cy3-DONs. MCF-7 cells expressed EGFR tagged with eGFP. The cells were incubated with a primary IgG antibody directed against phosphorylated EGFR (anti-phosphoEGFR, or αP-EGFR) and an Alexa Fluor 647-labeled secondary IgG antibody (αP-EGFR-IgG^{647}). Scale bars: 10 μm. (d) The cell response triggered by the four designed DON_F was measured by the 647-channel intensity ratio of phosphorylated-EGFR to DON signal, accounting for variations in DON_F immobilization and antibody staining. *P*-values were obtained from Kruskal–Wallis tests. ***$P < 0.001$.

one-pot DON_F/STV incubation outside the fluidic chip, (ii) sequential incubation in the fluidic chip under static incubation conditions, and (iii) sequential incubation in the fluidic chip with STV flowing at 10 μL/min. Although we have recently highlighted the benefits of using bidentate biotinylated linkers, which facilitate near-full occupancies for cell signaling studies,[19] we here intentionally employed conventional biotinylated linkers to work out the effects of fluidic incubation in more detail. Figure 3d shows the STV occupancy values for the three conditions. The average occupancy for DON_F incubated with STV outside fluidic chip (i) is 65.4 ± 1.1%. This value increases to 67.2 ± 0.5% when incubated with STV inside the chip under static conditions (ii) and to 70.3 ± 2.4% under constant flow (iii). Decoration within the chamber, even without flow, enhances binding by exposing ordered DONs to the STV solution, likely reducing the probability of unsuccessful collisions. Additionally, the convective supply of STV decreases the depletion layer, as previously discussed, resulting in higher binding levels. Thus, sequential decoration using the microfluidic device helps to improve ligand occupancy on the DONs.

Once the surface functionalization was optimized, we proceeded with cell studies. To do so, the STV-decorated DON_F were used to bind biotinylated DNA-antibody conjugates, which can bind to the EGF receptor (EGFR) in the membrane of live MCF-7 cells (Figure 4a). Here, we used the monoclonal antibody Panitumumab, which was chemically coupled with a 24-mer oligonucleotide (see the Experimental Section for synthesis details). Panitumumab ($K_D = 5 \times 10^{-11}$ M)[39] binds EGFR with an affinity 4 orders of magnitude higher than EGF ($K_D = 1.77 \times 10^{-7}$ M), thus preventing EGF binding.[40] Previous studies have shown that antibodies that bind EGFR laterally (not on the EGF binding site) can induce EGFR activation through clustering when attached to a surface.[41] We speculated that Panitumumab might also induce EGFR activation by receptor recruitment, even though it blocks the EGF binding site.

To streamline the experimental procedure, we continued using inkjet spotting to produce 80 μm diameter spots for cell interaction studies. This approach contrasts with previous works by simplifying the methodology as it overcomes the complexity of producing micropatterns smaller than 5 μm, which are often used for analyzing cell activation.[5,30] We here employed genetically modified MCF-7 cells overexpressing EGFR fused to eGFP for fluorescence visualization.[5,30,42] Cells were harvested in FBS (fetal bovine serum)-free medium enriched with β-estradiol to promote survival. The cells were then allowed to adhere to spots bearing DON_F, decorated with DNA-Panitumumab conjugates, coimmobilized with RGD (Arg–Gly–Asp) motifs to ensure efficient adhesion and spreading (Figures 4a and S9). Negative controls with DON_F lacking functional biomolecules confirmed minimal cell attachment (Figure S10).

After ensuring proper cell adhesion, we assessed EGFR activation triggered by DON_F with DNA-Panitumumab conjugates spaced at 24, 36, 48, and 60 nm. Figure 4b shows the AFM topographical images of these constructs. Cells were incubated for 15 min to prevent migration, then fixed, permeabilized, and immunostained with a primary antibody targeting activated (phosphorylated) EGFR, followed by an Alexa Fluor 647-labeled secondary antibody (αP-EGFR-IgG^{647}), providing thus a detectable fluorescent signal for TIRF microscopy (Figure 4c). Using ImageJ automatic analysis (Figure S11 and Table S3), we quantified the 647-channel intensity ratio of the phosphorylated EGFR to DON signal, which accounts for variations in DON_F immobilization and antibody staining. Note that the secondary antibody used for immunostaining shows cross-reactivity against human IgG and Panitumumab is a fully human IgG2 antibody, therefore nonspecific immunostaining on the DONs correlates with the

https://doi.org/10.1021/acsami.4c10874
ACS Appl. Mater. Interfaces 2024, 16, 53489–53498

amount of DON/Panitumumab immobilized on the surface. In this line, negative controls showed minimal nonspecific staining in surfaces lacking the primary antibody (Figure S12). Overall, Figure 4d indicates effective EGFR activation by DON_F with DNA-Panitumumab conjugates. Closer spacings (24 nm) resulted in higher intensities, suggesting a more efficient EGFR cluster formation. Increased spacings (36, 48, 60 nm) led to decreased activation, consistent with our previous hypothesis that optimal ligand spacing enhances receptor activation by matching the size of the EGFR clusters formed in the cell membrane.[30]

Therefore, to further validate our platform, we tested it with ligand arrangements similar to those described by Mayer et al., who used DON_{RT} with spacings of 6, 18, 30, 42, and 54 nm.[30] Here, we also found that EGFR activation in MCF-7 cells varied significantly with the spacing of the DNA-Panitumumab conjugates. Activation improved starting at 18 nm, whereas distances higher than 42 nm showed reduced effectiveness (Figure S13), thus being in alignment with the previous study. Specifically, optimal activation was observed at 30 and 42 nm, probably due to stable EGFR oligomer formation, while shorter (6, 18 nm) and longer distances (54 nm) reduced cell response, presumably by preventing effective clustering.[30]

Although our system demonstrated similar trends with different cells, ligands, and readouts, DON_{RT} results showed reduced sensitivity compared to those of Mayer et al., likely due to the use of larger spots, which resulted in signal averaging over whole cells. The use of micropatterns smaller than cells might therefore enhance signal specificity.[30] Of note, the flexibility of the DNA-Panitumumab conjugates allowed for effective binding over a range of distances, slightly differing from the fixed distances described in previous works.[5,14,19,30] The 8.2 nm DNA strand length, combined with a 45° rotational angle, enables a positioning range of ±5.8 nm per conjugate. For example, an 18 nm spacing between binding sites can extend to 29.5 nm when neighboring DNA-Panitumumab conjugates move 45° laterally. It is also relevant to note that the cells used here do not naturally express EGFR. Therefore, they do not rely on this receptor to grow and survive and are not significantly affected by the EGFR inhibitor Panitumumab. Consequently, using Panitumumab to induce EGFR clustering in this modified cell line is of limited clinical relevance.

Altogether, our system simplifies the experimental process and provides new relevant information showing that variations in the nanoscale distances of ligands on surface-immobilized DONs affect EGFR activation and clustering through inhibitory antibody-based interactions.

The platform described here promises to advance cellular studies by enabling real-time observation of surface functionalization and automatic quantification of EGFR activation through immunostaining. Ultimately, the platform could enhance our ability to control and study cell activation in diverse cell lines at the molecular level in a microfluidic environment. Beyond the proof-of-concept described here with MCF-7 cells overexpressing EGFR, future applications could involve testing the platform to investigate the effect of EGFR clustering driven by surface-immobilized Panitumumab-DNA conjugates in colorectal cancer cell lines such as HT29, SW48, and HCT116. These lines are commonly used to study the efficacy and mechanisms of EGFR inhibition by Panitumumab in solution.[43]

CONCLUSIONS

In this study, we developed a robust microfluidic platform that facilitates the real-time monitoring and precise functionalization of glass surfaces with DONs. By integrating controlled flow conditions with a TIRF microscope, we achieved a detailed kinetic analysis of DON immobilization on DNA-functionalized surfaces. Our results demonstrated significant influences of DON morphology and the nature of binding tags on hybridization efficiency, with twist-corrected DONs exhibiting notably higher efficiencies compared with their twisted counterparts. Comparative studies with the well-established SPR technique revealed that our microfluidic chamber's larger dimensions led to higher hybridization efficiencies for DONs, which are characterized by low diffusivity. The platform's capability for dynamic decoration of DONs allowed for in situ investigation of ligand occupancy and production of high-quality bioactive surfaces under flow conditions. Additionally, the platform enabled the detailed study of EGFR recruitment in living MCF-7 cells through antibody-based interactions. Our findings revealed that varying distances between EGFR-targeting antibodies on DONs significantly influenced EGFR activation, with closer inter-ligand spacings (24 nm) resulting in higher activation levels.

The versatility of our platform allows for adaptation to various cell lines and experimental conditions, making it a valuable tool for a broad range of biological and biomedical research. Thus, this platform opens the door to real-time analysis of cell reactions, particularly of the dynamic processes of cell behavior in response to nanoscale ligand arrangements. Given the critical role of cell−surface receptors in cell signaling, understanding their regulation is essential for developing cell-based therapeutic strategies. Microfluidic systems, such as the one described here, can serve this purpose, specifically for developing physiologically relevant models. Moreover, for applications of DONs as functional biomaterials, it is increasingly relevant to study binding kinetics and dynamic processes in real-time with high spatial resolution, such as proved with our platform. The integration of automated signal quantification and potential for high-throughput signal quantification holds the promise for more efficient analysis of cellular responses.

EXPERIMENTAL SECTION

DONs Design. The rectangular DONs used in this work follow designs detailed in previous studies.[5,19,30] Twisted DONs (DON_T), designed as in described by Angelin et al.[5] but without biotins, are shown in Figure S2a. Twist-corrected DONs (DON_F) were designed as per Dominguez et al.[19] and used either without biotins (Figure S2b) or with various biotinylated staple patterns (Figure S2d−i). The "5 far" DON_F, with conventional biotinylated linkers, was used for streptavidin (STV) occupancy studies at different flow rates. Twisted (DON_{RT}, Figure S2c,j−n) followed the designed described in Mayer et al.[30] Twist-corrected DON rulers (DON_{RF}, Figure S2d) were created by alternately deleting two staples from DON_{RT}. DON_F with linkers spaced by 24, 36, 48, and 60 nm, as well DON_{RT} with spacings at 6, 18, 30, 42, and 54 nm, all have double biotinylated linkers. These DONs were decorated with STV and biotinylated DNA-Panitumumab conjugates for cell studies. Nine or ten positions on the lower side of all DONs were selected for single-stranded binding tags, allowing immobilization on a solid surface via hybridization with surface-bound capture oligonucleotides (highlighted in red in Figure S2). The selected staples were elongated by 24 bases using sequence CAT or cF1 (Table S2). On the upper side of all DONs, 20 positions were chosen for Cy3 fluorophores. "Lower" and "upper side" refer to their positions on the DON plane after surface binding. The

https://doi.org/10.1021/acsami.4c10874
ACS Appl. Mater. Interfaces 2024, 16, 53489−53498

dimensions of DON_{RT} and DON_{RF} are 40 × 252 nm^2, while DON_T and DON_F measure 70 × 100 nm^2. Unmodified staple strand sequences are found in previous studies.[5,19,30] All modified sequences reported here are available upon request.

DON Assembly, Purification, and Quantification. All DONs were assembled using a 1:10 molar ratio of scaffold strand p7560 to staple strands as previously detailed.[19,30] The assembly took place in TE-Mg 7 buffer (20 mM Tris base, 1 mM EDTA, 7 mM $MgCl_2$, pH 7.6 adjusted with HCl) in a total volume of 500 μL. The process was conducted on a thermocycler (Eppendorf Mastercycler pro) with a stepwise temperature decrease from 75 to 25 °C. After an initial denaturation at 95 °C for 5 min, the temperature was reduced by 1 °C per cycle for 50 cycles, with each step held for 10 s. Following the procedure described,[19] DONs were purified using PEG precipitation by mixing with an equal volume of precipitation buffer (5 mM Tris base, 1 mM EDTA, 505 mM NaCl, 15% PEG-8000) and centrifuging at 16,100 g for 30 min. The resulting pellet was resuspended in 50 μL of TE-Mg 6 buffer (20 mM Tris base, 1 mM EDTA, and 6 mM $MgCl_2$, pH 7.6). The concentration of purified DONs was determined by quantitative polymerase chain reaction as previously described.[5]

SPR Spectroscopy Measurements. For SPR spectroscopy, a BIAcore X-100 instrument (Cytiva) with an SA sensor chip (Cytiva) was used. The surface of the SA sensor chip contains a dextran matrix with immobilized STV, which allows for the binding of biotinylated ligands. To measure the hybridization efficiency of DON_{RF} and DON_{RT} under various flow conditions, biotinylated capture oligonucleotides complementary to the DON protruding strands were first bound onto the SA chip. The capture oligonucleotides were injected in TE-NaCl 750 running buffer (20 mM Tris base, 1 mM EDTA, and 750 mM NaCl, pH 7.6) at a concentration of 50 nM and flushed over the active flow cell at 10 μL/min until a signal increase of 85 RU was registered. For the removal of any nonspecific bound biotinylated oligonucleotides, the chip surface was subsequently washed with three 30 s injections of 50 mM NaOH. Next, the reversible binding of DONs to the capture strands was tested. DONs at a concentration of 2 nM in TE-NaCl 750 running buffer were flushed over both the active flow cells with bound capture oligonucleotides and the empty reference flow cell at three different flow rates (1, 10, and 30 μL/min). For each flow rate, the contact and dissociation time was determined by the constraints of the instrument. For a flow rate of 1 μL/min, contact and dissociation time of 3600 s each was chosen. For 10 μL/min, this time was reduced to 540 s and for a flow rate of 30 μL/min, both the association and dissociation time was set to 180 s. Between different flow rates, all bound DONs were removed by flushing the reference and active flow cells with 70 mM NaOH for 120 s at a rate of 10 μL/min. All flow rates were tested twice for both DON constructs.

DNA−Protein Conjugate Synthesis. The synthesis of the DNA−protein conjugates was performed following established methods.[42,44] Briefly, for biotinylated DNA-Panitumumab conjugates, thiolated DNA [100 μM, 100 μL, sequence: (5′-dual biotin) CATCATCATCATCATCATCATCATCATCATCATCAT-CATCATCATCAT (Thiol C6−3′)] was incubated with TCEP (2 μL, 0.5 M) for 2 h at 30 °C, followed by gel filtration purification. Simultaneously, Panitumumab (Vectibix, 20 mg/mL, 133 μL) was incubated with Sulfo-SMCC (100 mM in DMSO, 5.3 μL) for 45 min at 30 °C and purified by gel filtration. The activated antibody was then reacted with the purified DNA for 2 h at room temperature or overnight at 4 °C. The mixture was further purified using anion-exchange chromatography on a Mono Q 5/50 column with a gradient of TRIS A (25 mM Tris−Cl, pH 8) and Tris B (25 mM Tris−Cl, 1 M NaCl, pH 8) buffers. Likewise, for DNA-STV conjugates, 100 μM STV was modified with maleimide groups using sSMCC and reacted with reduced thiolated DNA [100 μM, sequence: (5′-thiol C6) GTACTTCCTTAAACGACGCAGG-3′]. Purification was achieved through gel filtration and anion-exchange chromatograph. UV−vis spectroscopy was used to determine the concentrations of all DNA−protein conjugates.

Chemical Treatment of Glass Slides. The cleaning and chemical modification of glass slides followed established protocols.[5] Briefly, high-precision microscope glass slides (170 μm thick) were cleaned with 14.3% NH_3 and 14.3% H_2O_2 in double distilled water (ddH_2O) at 150 °C for 20 min. They were then rinsed with ddH_2O, ethanol, ddH_2O again, and dried using a N_2 stream. The dried glasses were then silanized with a 1% APTES (3-aminopropyltriethoxysilane) solution (95% methanol, 5% ddH_2O, 1 mM acetic acid) for 20 min. Afterward, the glasses were washed with ethanol, ddH_2O, and acetone before being dried under N_2. Finally, the glasses were incubated overnight in an acetone solution containing 5% PBAG [poly-(bisphenol A-*co*-epichlorohydrin), glycidyl end-capped] at room temperature. After incubation, they were washed with acetone, dried with N_2, and stored under a vacuum at −20 °C.

Micropatterning of the Glass Surface. Depending on the DON protruding tags, a 10 μM solution of the complementary capture oligonucleotide sequence aF1 (5′-NH_2-C12-TTTTTTTTCCTGCGTCGTTT-3′) or aATG (5′-NH_2-C6-TTTTTTTTATGATGATGATG-3′) in trehalose buffer (200 mM K_2HPO_4, 200 mM KH_2PO_4, 0.5% trehalose dehydrate, pH 7.6) was inkjet printed on epoxy-reactive glass slides using a NanoPlotter 2.1 (GeSiM). For immobilizing DON_{RT} in cell experiments, we used 5′-CCTGCGTCGTTTAAGGAAGTAC-C12-NH_2-3′. The solution was dispensed in 120 μL drops from a Pico-Tip J pressure tip, producing spots approximately 80 μm in diameter with a 200 μm pitch between spots. Each drop formed a single spot. The spotting was performed at 21 °C with 60% humidity.

Fluidic Chamber Fabrication and Assembly. A master mold containing the positive replicate of the chamber was designed using Computer-Aided Design and transferred to a micromill via Computer-Aided Manufacturing to be micromilled in a poly(methyl methacrylate) (PMMA) block. The master mold was then used to replicate the negative structure in PDMS (polydimethylsiloxane) through replica molding. The PDMS structure, containing the fluidic chamber, was glued with biocompatible silicone glue (ASC Applied Silicon Corporation) to the glass slide prepatterned with ssDNA capture strands and allowed to dry overnight.

Finite Element Methods (FEM) Simulation of Fluidic Mechanics in the Microfluidic Chamber. Numerical simulation of fluid mechanics was conducted by FEM with COMSOL Multiphysics software (version 6.1) to investigate the velocity profile within the fluidic chamber and the adsorption of chemical species onto a reactive surface. For this, the "laminar flow" and "transport of diluted species" modules were used. To simplify the simulation, it was assumed that the flowing species (DONs) experience a "fast irreversible surface reaction" ($V_c = -1$). Layered meshing operations were implemented to estimate the velocity at specific heights from the lower surface. All simulations were performed with a 2D cut of the channel (details in Figure S4).

Hybridization Tests. To optimize fluidic parameters for high-quality DON-decorated surfaces, we studied DON hybridization under various conditions. For flow rate testing, DON_F without biotins and with protruding binding tags cF1 were prepared at 2 nM in TE-NaCl 750 buffer with flow rates of 0, 10, 50, and 100 μL/min. For protruding staples testing, DON_F without biotins and with protruding binding tags CAT or cF1 were prepared at 2 nM in TE-NaCl 750 while maintaining a flow rate of 10 μL/min. In the comparison of twisted versus twist-corrected DONs, both types without biotins were prepared with protruding binding tags CAT and cF1 at 2 nM in TE-NaCl 750 with a flow rate of 10 μL/min. In DON ruler experiments, both DON_{RT} and DON_{RF} rulers were tested with CAT at 2 nM in TE-NaCl 750 under 10 μL/min. Images were taken with a Zeiss Elyra P.1 microscope with a Plan-Apochromat 63×/1.46 oil-immersion objective in TIRF mode at intervals of 0, 2, 4, 6, 8, 10, 14, 18, 22, and 26 min. Images were captured with an Andor iXon 897 back-thinned EM-CCD camera. Fluorescence intensity was analyzed using ImageJ (Fiji), and relative fluorescence intensity $\Delta F/F_0$ was plotted. This value was calculated by measuring the fluorescence intensity at a given time point (F), comparing it to the initial background intensity (F_0), and normalizing the difference (ΔF) relative to the initial intensity. Each experiment was performed in duplicates.

https://doi.org/10.1021/acsami.4c10874
ACS Appl. Mater. Interfaces 2024, 16, 53489−53498

Optimization of the Sequential Surface Functionalization. A three-step process was conducted to test the sequential functionalization of the surface under continuous flow conditions. First, 2 nM Cy3-DON_F with "5-far" biotin tags and CAT ligands were perfused onto the chip, which contained spots with ATG capture oligonucleotides. Next, 0.3 μM Cy5-STV was applied to bind specifically to the biotin ligands on surface-captured DON_F. Finally, 100 nM Dy405-labeled biotinylated ssDNA was introduced to bind to the immobilized STV. All steps were performed at a flow rate of 10 μL/min, with a surface wash with TE-NaCl 750 buffer in between steps. To assess the efficiency of nanopattern formation on the DON_F under this continuous flow condition, we compared STV occupancy against two other scenarios: one-pot incubation, where STV was incubated with DON_F outside the fluidic chip before the mixture was flowed at 10 μL/min, and static incubation of STV within the fluidic chip after DON_F immobilization. For these STV occupancy measurements, a photocleavable linker within the capture oligonucleotide anchored to the surface was used to release the DON_F-STV constructs. The surface was irradiated with UV light (λ = 312 nm) for 40 min, and the released DONs were measured using AFM.

AFM Analysis. DON_F-STV constructs were analyzed by AFM. Samples were diluted in TE-Mg 12.5 buffer (20 mM Tris base, 1 mM EDTA, 12.5 mM $MgCl_2$, pH 7.6) up to 20 times, depending on the sample concentration. 10 μL of the diluted samples was deposited on a freshly cleaved mica surface (Plano GmbH) and allowed to adsorb at room temperature for 3 min. After 50 μL of TE-Mg 12.5 buffer was added, the samples were imaged with pyramidal tips (SNL-10 tips, radius 2 nm, spring constant 0.35 N/m, Bruker) using a NanoWizard 3 atomic force microscope (JPK) in force-curve based imaging mode (QI). The images were analyzed by using JPK data processing software.

Cell Culture and Experimental Preparation. MCF-7 breast cancer cells, stably expressing EGF receptor (EGFR) fused to eGFP, were obtained from the Max-Planck Institute for Molecular Physiology.[5] Cells were harvested at 80% confluency, grown at 37 °C with 5% CO_2, and cultured in Eagle's Minimum Essential Medium (EMEM) with 1% GlutaMAX, 1% Pen/Strep, 10% FBS, and 0.6% G418 disulfate salt. For experiments, cells were washed with PBS−/− and dissociated using 2 mL of cold Accutase for 5 min. The cells were then resuspended in FBS-free EMEM, enriched with 50 pM β-estradiol to enhance cell survival, at a concentration of 300,000 cells/mL.

Surface Functionalization for Cell Experiments. All functionalization steps for cell experiments were performed under sterile conditions, and all washing steps used TE-NaCl 750 buffer. These experiments included DON_F and DON_{RT} with cF1 for surface immobilization and glass surfaces with micropattern spots presenting aF1. The inkjet-printed surface assembled in the microfluidic chamber was washed with buffer and then blocked with BSA (50 mg/mL BSA in TE-NaCl 750, denatured for 2 min at 95 °C) for 1 h to minimize nonspecific binding. Simultaneously, 5 pM cF1-STV conjugates and 100 pM biotin-RGD were mixed in TE-NaCl 750. Following the BSA block, the surface was washed and incubated with the cF1-STV and biotin-RGD mixture for another hour to promote cell adhesion on the spots. During this time, 2 nM DON_F were mixed with 0.3 μM STV in 50 μL TE-NaCl 750. For DON rulers, 1 nM DON_{RT} were combined with 0.15 μM STV in 50 μL TE-NaCl 750. The surface was washed and then treated with the DON-STV mixture for 1 h. While the surface was incubating with the DON-STVs mixture, 100 nM of biotinylated DNA-Panitumumab conjugates were mixed with 2.5 μM of the complementary DNA sequence (5′-ATGATGATGATGATGATGATG-3′) in 40 μL TE-NaCl 750. This step aimed to increase the rigidity of the DNA conjugate structure and ensure precise ligand positioning. The surface was washed before introducing the DNA-Panitumumab mixture for 1 h, then rinsed again with TE-NaCl 750 and finally with PBS+/+. Negative controls included DONs without ligands, DON decorated with STV but not incubated with the DNA-Panitumumab conjugate, and DON exposed to the biotinylated DNA-Panitumumab conjugate without prior incubation with STV.

Cell Experiments and Immunostaining. Following functionalization, the surface was incubated with a cell suspension of 300,000 cells/mL in FBS-free EMEM supplemented with 50 pM β-estradiol for 15 min to allow cell survival and adhesion while avoiding migration. Subsequently, adhered cells were fixed with 4% formaldehyde in PBS+/+ for 15 min, washed with PBS+/+, permeabilized with 0.1% Triton-X for 3 min, and then washed again with PBS+/+. Cell were immunostained by incubation with antibodies (Ab) against phosphorylated EGFR [Abcam, ab32430, anti-EGFR (phospho Y1068) Ab (Y38)] at a dilution of 1:300 in PBS+/+ with 5% BSA for 1 h. After washing with PBS+/+, the surface was incubated with goat antirabbit 647 Ab [Invitrogen, A-21244, IgG (H + L) cross-adsorbed secondary Ab, Alexa Fluor 647] at a dilution of 1:500 in PBS+/+ with 5% BSA overnight. Finally, the surface was washed with PBS+/+ before the microscopy analysis. Imaging was conducted in TIRF mode. The microscope used motorized adjustments for the TIRF angle, illuminating an area of 125 × 125 μm. Excitation sources included 488, 561, and 642 nm lasers.

Quantification of Fluorescent Signals for Cell Experiments. Fluorescent signals from TIRF images were automatically detected and quantified using an ImageJ-based macro (Table S3). The macro included instructions for defining regions of interest (ROIs) using thresholding algorithms. These ROIs comprised the area of the spot, the area of the cell, the area of the cell that colocalizes with the spot, and the area of the spot excluding the cell. After defining all ROIs, the macrometer measured the intensity of the 647-channel in both the colocalized area and the area of the spot excluding the cell (Figure S11). It then calculated the ratio of intensity between these two areas to correct for variations in DON and ligand quantities due to interactions between the cross-absorbed secondary antibody and Panitumumab.

Statistical Analysis. Data from all optimization tests are presented as mean ± SD. To assess variability between slides, at least ten spots were measured at the end of each test. In cell experiments, individual cell data are represented as dots, overlaid with box plots showing the 25th and 75th percentiles and the median. Each experimental condition was carried out in quadruplicates and included at least 160 analyzed cells (approximately 40 cells per replicate). Statistical analyses in SPSS software included the Mann−Whitney U test for comparisons between two groups and the Kruskal−Wallis test for comparisons among more than three groups, both chosen due to the non-normal distribution of the data. The resulting P-values are presented in Table S4.

■ ASSOCIATED CONTENT

Supporting Information

The Supporting Information is available free of charge at https://pubs.acs.org/doi/10.1021/acsami.4c10874.

Assembly of the fluidic setup; design of DON; time-lapse DON hybridization followed by TIRF microscopy; DON hybridization and depletion layer at different flow rates; root mean square fluctuations simulations for DONs; flow immobilization of DONs with different flexibility and binding tags; flow hybridization of DON rulers; DON release from surface; cell experiments without RGD anchors in FBS-free medium; cell experiments with RGD anchors and β-estradiol in FBS-free medium; automatic analysis pipeline for quantifying EGFR activation; negative controls accounting for non-specific staining; cell experiments with DON rulers; summary of cell signaling studies with DONs; protruding binding oligos for DONs; macro details for cell recognition and EGFR signal quantification; and statistical test details (PDF)

https://doi.org/10.1021/acsami.4c10874
ACS Appl. Mater. Interfaces 2024, 16, 53489−53498

AUTHOR INFORMATION

Corresponding Author

Carmen M. Domínguez − *Institute for Biological Interfaces (IBG-1), Karlsruhe Institute of Technology (KIT), 76344 Eggenstein-Leopoldshafen, Germany;* orcid.org/0000-0002-0918-5473; Email: carmen.dominguez@kit.edu

Authors

Miguel García-Chamé − *Institute for Biological Interfaces (IBG-1), Karlsruhe Institute of Technology (KIT), 76344 Eggenstein-Leopoldshafen, Germany*

Ivy Mayer − *Institute for Biological Interfaces (IBG-1), Karlsruhe Institute of Technology (KIT), 76344 Eggenstein-Leopoldshafen, Germany;* orcid.org/0000-0002-6868-9719

Leonie Schneider − *Institute for Biological Interfaces (IBG-1), Karlsruhe Institute of Technology (KIT), 76344 Eggenstein-Leopoldshafen, Germany;* orcid.org/0000-0002-3772-1480

Christof M. Niemeyer − *Institute for Biological Interfaces (IBG-1), Karlsruhe Institute of Technology (KIT), 76344 Eggenstein-Leopoldshafen, Germany*

Complete contact information is available at: https://pubs.acs.org/10.1021/acsami.4c10874

Author Contributions

CMD and CMN conceived the idea of the project. CMD, MGC, and IM performed the experiments. LS synthesized the Panitumumab-DNA conjugates. CMD performed the simulations. CMD, MGC, and CMN wrote the manuscript. The manuscript was written through contributions of all authors. All authors have given approval to the final version of the manuscript.

Funding

This work was financially supported through the Marie Sklodowska-Curie Individual Fellowship program of the European Commission (H2020-MSCA-IF, grant number 746713, recipient: CMD); the Alexander von Humboldt Postdoctoral Fellowship program of the Alexander von Humboldt Foundation (recipient: CMD); the Helmholtz program "Materials Systems Engineering" under the topic "Adaptive and Bioinstructive Materials Systems"; and the Deutsche Forschungsgemeinschaft (GRK 2039).

Notes

The authors declare no competing financial interest.

REFERENCES

(1) Rothemund, P. W. K. Folding DNA to create nanoscale shapes and patterns. *Nature* **2006**, *440*, 297−302.

(2) Dey, S.; Fan, C.; Gothelf, K. V.; Li, J.; Lin, C.; Liu, L.; Liu, N.; Nijenhuis, M. A. D.; Saccà, B.; Simmel, F. C.; et al. DNA origami. *Nat. Rev. Methods Primers* **2021**, *1*, 13.

(3) Knappe, G. A.; Wamhoff, E. C.; Bathe, M. Functionalizing DNA origami to investigate and interact with biological systems. *Nat. Rev. Mater.* **2022**, *8*, 123−138.

(4) Shaw, A.; Lundin, V.; Petrova, E.; Fordos, F.; Benson, E.; Al-Amin, A.; Herland, A.; Blokzijl, A.; Hogberg, B.; Teixeira, A. I. Spatial control of membrane receptor function using ligand nanocalipers. *Nat. Methods* **2014**, *11*, 841−846.

(5) Angelin, A.; Weigel, S.; Garrecht, R.; Meyer, R.; Bauer, J.; Kumar, R. K.; Hirtz, M.; Niemeyer, C. M. Multiscale Origami Structures as Interface for Cells. *Angew. Chem., Int. Ed.* **2015**, *54*, 15813−15817.

(6) Hawkes, W.; Huang, D.; Reynolds, P.; Hammond, L.; Ward, M.; Gadegaard, N.; Marshall, J. F.; Iskratsch, T.; Palma, M. Probing the nanoscale organisation and multivalency of cell surface receptors: DNA origami nanoarrays for cellular studies with single-molecule control. *Faraday Discuss.* **2019**, *219*, 203−219.

(7) Huang, D.; Patel, K.; Perez-Garrido, S.; Marshall, J. F.; Palma, M. DNA Origami Nanoarrays for Multivalent Investigations of Cancer Cell Spreading with Nanoscale Spatial Resolution and Single-Molecule Control. *ACS Nano* **2019**, *13*, 728−736.

(8) Veneziano, R.; Moyer, T. J.; Stone, M. B.; Wamhoff, E. C.; Read, B. J.; Mukherjee, S.; Shepherd, T. R.; Das, J.; Schief, W. R.; Irvine, D. J.; et al. Role of nanoscale antigen organization on B-cell activation probed using DNA origami. *Nat. Nanotechnol.* **2020**, *15*, 716−723.

(9) Verheyen, T.; Fang, T.; Lindenhofer, D.; Wang, Y.; Akopyan, K.; Lindqvist, A.; Högberg, B.; Teixeira, A. I. Spatial organization-dependent EphA2 transcriptional responses revealed by ligand nanocalipers. *Nucleic Acids Res.* **2020**, *48*, 5777−5787.

(10) Hellmeier, J.; Platzer, R.; Eklund, A. S.; Schlichthaerle, T.; Karner, A.; Motsch, V.; Schneider, M. C.; Kurz, E.; Bamieh, V.; Brameshuber, M.; et al. DNA origami demonstrate the unique stimulatory power of single pMHCs as T cell antigens. *Proc. Natl. Acad. Sci. U.S.A.* **2021**, *118*, No. e2016857118.

(11) Berger, R. M. L.; Weck, J. M.; Kempe, S. M.; Hill, O.; Liedl, T.; Radler, J. O.; Monzel, C.; Heuer-Jungemann, A. Nanoscale FasL Organization on DNA Origami to Decipher Apoptosis Signal Activation in Cells. *Small* **2021**, *17*, No. e2101678.

(12) Dong, R.; Aksel, T.; Chan, W.; Germain, R. N.; Vale, R. D.; Douglas, S. M. DNA origami patterning of synthetic T cell receptors reveals spatial control of the sensitivity and kinetics of signal activation. *Proc. Natl. Acad. Sci. U.S.A.* **2021**, *118*, No. e2109057118.

(13) Comberlato, A.; Koga, M. M.; Nüssing, S.; Parish, I. A.; Bastings, M. M. C. Spatially Controlled Activation of Toll-like Receptor 9 with DNA-Based Nanomaterials. *Nano Lett.* **2022**, *22*, 2506−2513.

(14) Lanzerstorfer, P.; Müller, U.; Gordiyenko, K.; Weghuber, J.; Niemeyer, C. M. Highly Modular Protein Micropatterning Sheds Light on the Role of Clathrin-Mediated Endocytosis for the Quantitative Analysis of Protein-Protein Interactions in Live Cells. *Biomolecules* **2020**, *10*, 540.

(15) Hellmeier, J.; Platzer, R.; Mühlgrabner, V.; Schneider, M.; Kurz, E.; Schütz, G. J.; Huppa, J.; Sevcsik, E. Strategies for the Site-Specific Decoration of DNA Origami Nanostructures with Functionally Intact Proteins. *ACS Nano* **2021**, *15*, 15057−15068.

(16) Wang, Y.; Baars, I.; Fordos, F.; Hogberg, B. Clustering of Death Receptor for Apoptosis Using Nanoscale Patterns of Peptides. *ACS Nano* **2021**, *15*, 9614−9626.

(17) Fang, T.; Alvelid, J.; Spratt, J.; Ambrosetti, E.; Testa, I.; Teixeira, A. I. Spatial Regulation of T-Cell Signaling by Programmed Death-Ligand 1 on Wireframe DNA Origami Flat Sheets. *ACS Nano* **2021**, *15*, 3441−3452.

(18) Cremers, G. A. O.; Rosier, B.; Meijs, A.; Tito, N. B.; van Duijnhoven, S. M. J.; van Eenennaam, H.; Albertazzi, L.; de Greef, T. F. A. Determinants of Ligand-Functionalized DNA Nanostructure-Cell Interactions. *J. Am. Chem. Soc.* **2021**, *143*, 10131−10142.

(19) Dominguez, C. M.; Garcia-Chame, M.; Muller, U.; Kraus, A.; Gordiyenko, K.; Itani, A.; Haschke, H.; Lanzerstorfer, P.; Rabe, K. S.; Niemeyer, C. M. Linker Engineering of Ligand-Decorated DNA Origami Nanostructures Affects Biological Activity. *Small* **2022**, *18*, No. e2202704.

(20) Sun, Y.; Sun, J.; Xiao, M.; Lai, W.; Li, L.; Fan, C.; Pei, H. DNA origami-based artificial antigen-presenting cells for adoptive T cell therapy. *Sci. Adv.* **2022**, *8*, No. eadd1106.

(21) Wang, C. H.; Chen, X. Q.; Su, Y. Y.; Wang, H.; Li, D. Precise regulating T cell activation signaling with spatial controllable positioning of receptors on DNA origami. *Chin. J. Anal. Chem.* **2022**, *50*, 100091.

(22) Wang, M.; Yang, D.; Lu, Q.; Liu, L.; Cai, Z.; Wang, Y.; Wang, H. H.; Wang, P.; Nie, Z. Spatially Reprogramed Receptor

Organization to Switch Cell Behavior Using a DNA Origami-Templated Aptamer Nanoarray. *Nano Lett.* **2022**, *22*, 8445−8454.
(23) Frtús, A.; Smolková, B.; Uzhytchak, M.; Lunova, M.; Jirsa, M.; Henry, S. J. W.; Dejneka, A.; Stephanopoulos, N.; Lunov, O. The interactions between DNA nanostructures and cells: A critical overview from a cell biology perspective. *Acta Biomater.* **2022**, *146*, 10−22.
(24) Schneider, L.; Rabe, K. S.; Dominguez, C. M.; Niemeyer, C. M. Hapten-Decorated DNA Nanostructures Decipher the Antigen-Mediated Spatial Organization of Antibodies Involved in Mast Cell Activation. *ACS Nano* **2023**, *17*, 6719−6730.
(25) Wagenbauer, K. F.; Pham, N.; Gottschlich, A.; Kick, B.; Kozina, V.; Frank, C.; Trninic, D.; Stommer, P.; Grunmeier, R.; Carlini, E.; et al. Programmable multispecific DNA-origami-based T-cell engagers. *Nat. Nanotechnol.* **2023**, *18*, 1319−1326.
(26) Platzer, R.; Hellmeier, J.; Göhring, J.; Perez, I. D.; Schatzlmaier, P.; Bodner, C.; Focke-Tejkl, M.; Schütz, G. J.; Sevcsik, E.; Stockinger, H.; et al. Monomeric agonist peptide/MHCII complexes activate T-cells in an autonomous fashion. *EMBO Rep.* **2023**, *24*, No. e57842.
(27) Wamhoff, E.-C.; Ronsard, L.; Feldman, J.; Knappe, G. A.; Hauser, B. M.; Romanov, A.; Case, J. B.; Sanapala, S.; Lam, E. C.; Denis, K. J. S.; et al. Enhancing antibody responses by multivalent antigen display on thymus-independent DNA origami scaffolds. *Nat. Commun.* **2024**, *15*, 795.
(28) Paloja, K.; Weiden, J.; Hellmeier, J.; Eklund, A. S.; Reinhardt, S. C. M.; Parish, I. A.; Jungmann, R.; Bastings, M. M. C. Balancing the Nanoscale Organization in Multivalent Materials for Functional Inhibition of the Programmed Death-1 Immune Checkpoint. *ACS Nano* **2024**, *18*, 1381−1395.
(29) Spratt, J.; Dias, J. M.; Kolonelou, C.; Kiriako, G.; Engström, E.; Petrova, E.; Karampelias, C.; Cervenka, I.; Papanicolaou, N.; Lentini, A.; et al. Multivalent insulin receptor activation using insulin−DNA origami nanostructures. *Nat. Nanotechnol.* **2024**, *19*, 237−245.
(30) Mayer, I.; Karimian, T.; Gordiyenko, K.; Angelin, A.; Kumar, R.; Hirtz, M.; Mikut, R.; Reischl, M.; Stegmaier, J.; Zhou, L.; et al. Surface-Patterned DNA Origami Rulers Reveal Nanoscale Distance Dependency of the Epidermal Growth Factor Receptor Activation. *Nano Lett.* **2024**, *24*, 1611−1619.
(31) García-Chamé, M.; Wadhwani, P.; Pfeifer, J.; Schepers, U.; Niemeyer, C. M.; Domínguez, C. M. A Versatile Microfluidic Platform for Extravasation Studies Based on DNA Origami—Cell Interactions. *Angew. Chem., Int. Ed.* **2024**, *63*, No. e202318805.
(32) Schneider, A. K.; Niemeyer, C. M. DNA Surface Technology: From Gene Sensors to Integrated Systems for Life and Materials Sciences. *Angew. Chem., Int. Ed.* **2018**, *57*, 16959−16967.
(33) Scheler, O.; Postek, W.; Garstecki, P. Recent developments of microfluidics as a tool for biotechnology and microbiology. *Curr. Opin. Biotechnol.* **2019**, *55*, 60−67.
(34) Tomov, T. E.; Tsukanov, R.; Glick, Y.; Berger, Y.; Liber, M.; Avrahami, D.; Gerber, D.; Nir, E. DNA Bipedal Motor Achieves a Large Number of Steps Due to Operation Using Microfluidics-Based Interface. *ACS Nano* **2017**, *11*, 4002−4008.
(35) Squires, T. M.; Quake, S. R. Microfluidics: Fluid physics at the nanoliter scale. *Rev. Mod. Phys.* **2005**, *77*, 977−1026.
(36) Karlsson, R. Biosensor binding data and its applicability to the determination of active concentration. *Biophys. Rev.* **2016**, *8*, 347−358.
(37) Ouldridge, T. E.; Šulc, P.; Romano, F.; Doye, J. P. K.; Louis, A. A. DNA hybridization kinetics: zippering, internal displacement and sequence dependence. *Nucleic Acids Res.* **2013**, *41*, 8886−8895.
(38) Ducloux, O.; Galopin, E.; Zoueshtiagh, F.; Merlen, A.; Thomy, V. Enhancement of biosensing performance in a droplet-based bioreactor by in situ microstreaming. *Biomicrofluidics* **2010**, *4*, 011102.
(39) Grothey, A.; Grothey, A. Targeting colorectal cancer with human anti-EGFR monoclonocal antibodies: focus on panitumumab. *Biol.: Targets Ther.* **2008**, *2*, 223−228.
(40) Kuo, W.-T.; Lin, W.-C.; Chang, K.-C.; Huang, J.-Y.; Yen, K.-C.; Young, I.-C.; Sun, Y.-J.; Lin, F.-H. Quantitative Analysis of Ligand-EGFR Interactions: A Platform for Screening Targeting Molecules. *PLoS One* **2015**, *10*, No. e0116610.
(41) Lanzerstorfer, P.; Borgmann, D.; Schütz, G.; Winkler, S. M.; Höglinger, O.; Weghuber, J. Quantification and Kinetic Analysis of Grb2-EGFR Interaction on Micro-Patterned Surfaces for the Characterization of EGFR-Modulating Substances. *PLoS One* **2014**, *9*, No. e92151.
(42) Hu, Y.; Dominguez, C. M.; Christ, S.; Niemeyer, C. M. Postsynthetic Functionalization of DNA-Nanocomposites with Proteins Yields Bioinstructive Matrices for Cell Culture Applications. *Angew. Chem., Int. Ed.* **2020**, *59*, 19016−19020.
(43) Kügler, J. Panitumumab (Vectibix®): A Treatment for Metastatic Colorectal Cancer. In *Handbook of Therapeutic Antibodies*, 2014; pp 1855−1870..
(44) Wacker, R.; Niemeyer, C. M. Synthesis of covalent oligonucleotide-streptavidin conjugates and their application in DNA-directed immobilization (DDI) of proteins. *Curr. Protoc. Nucleic Acid Chem.* **2005**, *22*, 12.

https://doi.org/10.1021/acsami.4c10874
ACS Appl. Mater. Interfaces 2024, 16, 53489−53498